RSC Advances

PAPER

View Article Online
View Journal | View Issue

Check for updates

Cite this: *RSC Adv.*, 2022, **12**, 23912

Facile design and synthesis of a nickel disulfide/zeolitic imidazolate framework-67 composite material with a robust cladding structure for high-efficiency supercapacitors†

Ming-yuan Sun,[a] Hao Xu,[b] Yun-tong Meng,[a] Xue-Mei Chen,*[a] Min Lu,*[a] Hao Yu*[a] and Chun-Bo Zhang[c]

Received 13th July 2022
Accepted 9th August 2022

DOI: 10.1039/d2ra04317c

rsc.li/rsc-advances

In this paper, a core–shell structure nickel disulfide and ZIF-67 composite electrode material (NiS_2/ZIF-67) was synthesized by a two-step method. Firstly, spherical NiS_2 was synthesized by a hydrothermal method, dispersed in methanol, then reacted and coated by adding cobalt ions and 2-methylimidazole to obtain the NiS_2/ZIF-67 core–shell composite. The NiS_2/ZIF-67 composite shows a high specific capacitance (1297.9 F g^{-1} at 1 A g^{-1}) and excellent cycling durability (retaining 110.0% after 4000 cycles at 5 A g^{-1}). Furthermore, the corresponding hybrid supercapacitor (NiS_2/ZIF-67//AC HSC) has an energy density of 9.5 W h kg^{-1} at 411.1 W kg^{-1} (6 M KOH) and remarkable cycling stability (maintaining 133.3% after 5000 cycles). Its excellent electrochemical performance may be due to the core–shell structure and the synergistic effect between the transition metal sulfide and metal–organic framework. These results indicate that the NiS_2/ZIF-67 composite as an electrode material with a core–shell structure has potential application in high-efficiency supercapacitors.

1. Introduction

With the exploration of new energy resources and portable electronic equipment, clean energy and efficient energy storage equipment are also being actively developed, making a great contribution to the improvement of the environment.[1–6] As one of the most efficient energy storage devices with good prospects, supercapacitors (SCs) have attracted extensive research interest because of their advantages such as their low cost, high power density and rapid charging–discharging performance.[7,8] They have been widely applied in military, aerospace, civil transportation, electronic equipment and other fields.[9–11] However, their low energy density and rate performance are technical bottlenecks that are difficult to overcome, and greatly restrict their further popularization and application. There are mainly two effective ways to improve the energy density of supercapacitor systems. One is to improve the specific capacitance of the electrode material, and the other is the exploitation of asymmetric hybrid supercapacitors, using active carbon electrodes as one electrode and a pseudocapacitance electrode material or battery electrode material as the other.[12,13] At present, most researchers focus on positive materials with redox activity combined with activated carbon to improve the energy density of hybrid supercapacitors.[14,15] Therefore, the design and development of positive materials has been one of the hotspots in this field.

According to previous reports, transition metal compounds (TMCs) have excellent electrochemical properties because of their participation in rapid and reversible Faraday redox reactions. Recently, researchers have studied numerous TMCs as electrode materials for SCs, such as NiO,[16,17] MnO_2,[18,19] $Ni(OH)_2$,[20,21] $Co(OH)_2$,[22,23] CuS,[24,25] NiS[26,27] and NiS_2.[28,29] However, their poor electrical conductivity and low mechanical strength limit their application severely. Some effective and feasible strategies have been adopted to enhance the rate capability and improve the cycling stability of transition metal compounds. Mishra *et al.* compounded RuO_2 on sheet-like graphene by chemical deposition to obtain RuO_2/GO composites. The composite material used as a supercapacitor material has a specific capacitance of 220 F g^{-1} at 10 A g^{-1}.[30] Biny and co-workers prepared the petal-like α-$Ni(OH)_2$ by a hydrothermal method, with a specific capacitance of 516 F g^{-1} at 0.5 A g^{-1} and a retained rate of 84% after 1000 cycles.[31]

In addition to carbon materials, the reasonable and controllable introduction of MOFs as electrodes for SCs has attracted increasing attention. Yang *et al.* doped Co/Zn–Ni–MOF//CNTs–COOH nanomaterials with Co^{2+}/Zn^{2+} for 5000

---

[a] *School of Chemical Engineering, Northeast Electric Power University, Jilin 132000, P. R. China. E-mail: lumin19770919@163.com*

[b] *Xinjiang Shihezi Vocational Technical College, Xinjiang 832000, P. R. China*

[c] *Electric Power Research Institute of State Grid Jilin Electric Power Co., LTD, Jilin 132000, P. R. China*

† Electronic supplementary information (ESI) available. See https://doi.org/10.1039/d2ra04317c

cycles. After being assembled into a hybrid supercapacitor, their capacities retained 86% and 80% after 5000 cycles at 10 A g^{-1}, respectively.[32] These demonstrate that the electrode materials constructed by combining transition metal materials and metal–organic frameworks (MOFs) to construct electrode materials is expected to achieve higher electrochemical performance through synergistic effects. In addition, the results show that the larger the inner space of the hollow sphere, the better its physical and chemical properties, such as low density, large effective area, and good mass permeability. Thus, it has more active sites and faster charge transfer ability, which further improve the electrochemical properties of the material.[33–39] Various transition metal compounds with hollow sphere structures have been applied in different energy storage fields, such as NiS[40] and NiO.[41] The electrochemical performance of the materials largely depends on their chemical constitution and morphology.[42] Therefore, researchers are studying various composite materials with different morphologies. However, the introduction of MOF-derived materials to construct coating structures is rarely reported.

In this article, a simple strategy to synthesize novel NiS_2/ZIF-67 composites with hollow sphere structures was reported. Herein, NiS_2 with a structure containing hollow spheres was firstly prepared as a carrier by hydrothermal method, and a thin layer of ZIF-67 was then formed after resting on the outer surface of NiS_2 for some time. Finally, the materials were transformed into NiS_2/ZIF-67 composites by this method. In this process, the prepared NiS_2/ZIF-67 composites could inherit the spherical structure of the NiS_2 carriers. Moreover, the prepared NiS_2/ZIF-67 composite material was characterized in detail, and its performance as the positive electrode of a supercapacitor was evaluated. It was evident that the formation of the ZIF-67 thin layer greatly increased the specific surface area and active site of the material. The electrochemical characterization results show that the capacitance of the NiS_2/ZIF-67 composite was 1297.8 F g^{-1} at 1 A g^{-1}, which was much higher than that of NiS_2 and ZIF-67. After 4000 cycles, the specific capacitance retained 110.0% of the initial value. Its electrochemical properties are much better than those of other reported materials.

2. Experimental

2.1 Materials

All reagents are of analytical grade and do not require further purification. All of the experimental water used in this study was ultrapure water.

2.2 Synthesis of NiS_2 hollow spheres

1 mmol $Ni(NO_3)_2\cdot 6H_2O$ and 1 mmol urea were dissolved in 20 mL deionized water, then 4 mmol L-cysteine as the S^{2-} source and 50 mL deionized water were each added. The mixture was treated by ultrasound for a period of time, and the hydrothermal reaction was carried out at 120 °C for 24 h. The black precipitate was washed with distilled water and anhydrous ethanol for several times and dried at 60 °C for 12 h to obtain the hollow spherical NiS_2.[43]

2.3 Preparation of NiS_2/ZIF-67 and ZIF-67

1 mmol $Co(NO_3)_2\cdot 6H_2O$ and 4 mmol 2-methylimidazole (2-MIM) were dissolved in 20 mL methanol. Then, a certain amount of NiS_2 was added to 10 mL methanol by stirring and uniformly dispersed. The mixture of the two solutions was aged at room temperature for 24 h after the intense agitation. Finally, the product was cleaned with methanol several times to remove impurities, and dried at 60 °C for 12 h to obtain NiS_2/ZIF-67. Since the dosage of NiS_2 was 0.3, 0.5 and 0.7 mmol, the terms of 0.3-NiS_2/ZIF-67, 0.5-NiS_2/ZIF-67 and 0.7-NiS_2/ZIF-67 were used to represent the different contents of the composite materials in the following characterization and experiment, respectively. Moreover, as a comparison, only ZIF-67 nanocrystals were also synthesized through a nearly identical static process without using NiS_2.[44]

2.4 Characterization

The morphology and size of the products were characterized by scanning electron microscopy (SEM) with a JSM-6510A microscope and sputtering with gold. Transmission electron microscopy (TEM) was carried out on a FEI Tecnai G2 F20 S-TWIN transmission electron microscope. The samples were tested by X-ray diffraction (XRD-7000), recorded by a Shimadzu X-ray powder diffractometer with Cu-Kα radiation ($\lambda = 0.15405$ nm). X-ray photoelectron spectroscopy (XPS, ESCALAB-250) with an Al-Kα radiation source was adopted. The Brunauer–Emmett–Teller (BET) principle and N_2 adsorption–desorption measurements were carried out using an ASAP 2020 V4.01 system to determine the specific surface areas of the as-synthesized materials. The information on the chemical bonding was obtained by Fourier transformed infrared spectroscopy (FTIR, Nicolet iS50).

2.5 Test of the electrochemical properties

The classical three-electrode system (saturated Hg/HgO reference electrode, platinum counter electrode and working electrode) was used to study the electrochemical performance of the samples prepared on a CHI 660E type electrochemical workstation in 2 M KOH aqueous solution electrolyte. The working electrode was prepared by mixing the active material with acetylene black and polytetrafluoroethylene (PTFE) emulsion in ethanol at a mass ratio of 8 : 1 : 1. Then, the mixture of the fully ground to uniform black slurry was applied to the pretreated nickel foam (active material decoration area of 1.0 × 1.0 cm^2) at 8 MPa pressure for 30 seconds. Finally, the nickel foam containing the active materials was dried at 60 °C for 12 h. The electrochemical performances were assessed by cyclic voltammetry (CV), galvanostatic charge–discharge (GCD) measurements, and electrochemical impedance spectroscopy (EIS). The average specific capacitance (C_s, F g^{-1}) of the electrodes was calculated by eqn (1) according to the galvanostatic charge–discharge curves,[45]

$$C_s = \frac{I \times \Delta t}{\Delta V \times m} \tag{1}$$

where I (A), Δt (s), ΔV (V) and m (g) are the discharge current, discharge time, applied potential window and mass of the active material on the working electrode, respectively.

3. Results and discussion

3.1 Morphology and structure characterization

NiS_2 was synthesized by the hydrothermal reaction of nickel nitrate and L-cysteine. As is well shown in the XRD pattern (Fig. S1a†), all of the diffraction peaks point to the cubic phase NiS_2 (JCPDS card no. 89-1495). The characteristic peaks are narrow and sharp, demonstrating that the synthesized NiS_2 is phase-pure without impurity.[46] The morphology and microstructure of the materials are characterized by SEM. In Fig. S1b,† the morphology of NiS_2 is a hollow spherical structure with the diameter of about 2.33 μm, which is the same conclusion as previously reported.[47]

Subsequently, the crystallographic phase of the NiS_2/ZIF-67 materials was further measured by XRD, as shown in Fig. 1. The XRD pattern spectra of the NiS_2/ZIF-67 composites are similar to that of the simulated ZIF-67 structure between 5° and 30°. The diffraction peaks at $2\theta = 7.38°$, 10.46°, 12.82°, 16.56°, 18.16°, 22.28° and 24.68° are caused by the ZIF-67 structure.[48] The diffraction peaks at $2\theta = 31.48°$, 35.48°, 38.84°, 45.16° and 53.44° could be ascribed to the (200), (210), (211), (220) and (311) planes of cubic phase NiS_2, respectively. Therefore, the composite is composed of NiS_2/ZIF-67 based on the XRD results. It is worth noting that the peak in the NiS_2 part is not as intense as the peak in the ZIF-67 part. In addition, the peak intensity of the NiS_2 part in the different NiS_2/ZIF-67 composite materials increases continuously as the dosage of NiS_2 increases from 0.3 mmol to 0.7 mmol. This may be due to the coating of ZIF-67, as NiS_2 is unlikely to reflect many diffraction peaks. Toward proving this point and understanding the structure and morphology of NiS_2/ZIF-67, SEM characterization was carried out.

ZIF-67 particles are the shape of rhombic dodecahedrons with a side length of about 500 nm (Fig. 2a and b). In Fig. 2c, it can be seen that there is no obvious spherical structure when the dosage of NiS_2 is only 0.3 mmol. As shown in Fig. 2d and e, with the increasing moderate amount of NiS_2 introduced in the preparation of ZIF-67, the basic structure of the composite material is well inherited. Furthermore, a certain amount of ZIF-67 is covered on the surface of the spherical structure of NiS_2, and the spherical structure surface of NiS_2 changed from smooth to being full of wrinkles. Meanwhile, some ZIF-67 is scattered outside of the main structure. When the NiS_2 content reached 0.7 mmol (Fig. 2f), a small part of the hollow NiS_2 spheres was not covered by ZIF-67.

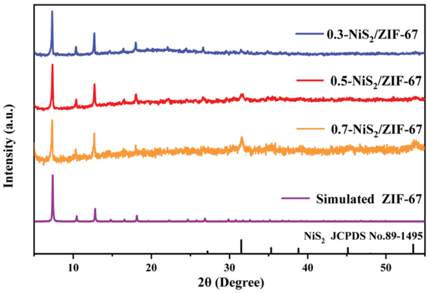

Fig. 1 XRD patterns of the synthesized products.

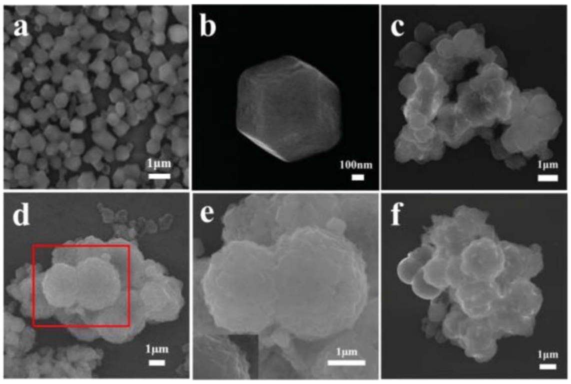

Fig. 2 SEM images of ZIF-67 (a and b), 0.3-NiS_2/ZIF-67 (c), 0.5-NiS_2/ZIF-67 (d and e) and 0.7-NiS_2/ZIF-67 (f).

The hollow spherical coating structure of 0.5-NiS_2/ZIF-67 was further studied by TEM, as shown in Fig. 3a and b. As presented in Fig. 3a, the contrast between the black edges and the white interior confirms the hollow structure of the spheres. From the partially enlarged image in Fig. 3b, the surface of NiS_2 is covered with a layer of rhomboid dodecahedron ZIF-67 with distinct interfaces. The TEM results are in good agreement with the SEM results. Furthermore, the EDS elemental mapping images shown in Fig. 3c obviously illustrate the uniform distribution of the Ni, Co and S elements in a hollow sphere, demonstrating the successful preparation of the NiS_2/ZIF-67 composite.

To identify the composition of the composite materials, an EDS measurement was carried out to confirm the presence and the approximate proportion of the Co, Ni and S elements. As shown in Fig. S2,† the EDS spectra of the 0.5-NiS_2/ZIF-67 composite further confirmed the existence of Ni, Co and S elements in the composite. The atomic mole ratio of Ni : Co : S

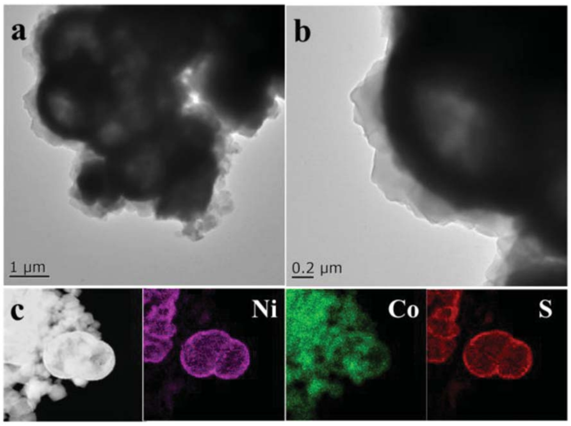

Fig. 3 TEM images of 0.5-NiS_2/ZIF-67 (a and b). EDS elemental mapping images of 0.5-NiS_2/ZIF-67 (c).

is about 1 : 3 : 2. The Ni/S ratio is very close to the stoichiometric ratio of NiS_2. The high content of the Co element may be attributed to the ZIF-67 scattered around.

The surface elemental and chemical composition of 0.5-NiS_2/ZIF-67 were characterized by XPS. The survey spectrum (Fig. S3a†) shows that 0.5-NiS_2/ZIF-67 consists of Ni, Co, O, C and S elements without other impurities. Two shake-up satellites and two main peaks are shown in the high-resolution XPS spectrum of Ni 2p (Fig. S3b†), which can be considered as the Ni $2p_{3/2}$ and Ni $2p_{1/2}$ orbitals of Ni^{2+}, respectively.[49] In addition, the high-resolution XPS spectrum of Co 2p (Fig. 4a) is consistent with two main peaks (Co $2p_{3/2}$ and Co $2p_{1/2}$) and two shake-up satellites (Sat.). These diffraction peaks indicate the presence of Co^{2+}.[50] In Fig. 4b, the C 1s spectra has three types of functional groups, which are C–OH (288.6 eV), C=O (286.0 eV) and C–C (284.6 eV). In this regard, it shows the main mode of each element.

It is of significance that the specific surface area of the electrode materials influence the electrochemical performance. The specific surface areas of NiS_2, ZIF-67 and NiS_2/ZIF-67 composites are determined by the N_2 adsorption–desorption isotherms. The specific BET surface areas of NiS_2 and ZIF-67 are 1.89 and 1360.10 $m^2\ g^{-1}$, respectively (Fig. S4†). In addition, the specific surface areas of 0.3-NiS_2/ZIF-67, 0.5-NiS_2/ZIF-67 and 0.7-NiS_2/ZIF-67 are 765.18, 577.16 and 547.70 $m^2\ g^{-1}$, respectively (Fig. 5). Compared with NiS_2, the specific surface area of the NiS_2/ZIF-67 composite is significantly increased. With the increase in the amount of NiS_2 introduced, the specific surface area decreases successively. Generally, the surface area was directly related to the high electrochemical performance.[51] The increased specific surface area is able to afford more active sites to improve the charge storage efficiency.[52] It can be inferred that the composition and surface area of the electrode material may be the key factors leading to the excellent charge storage performance.[53,54]

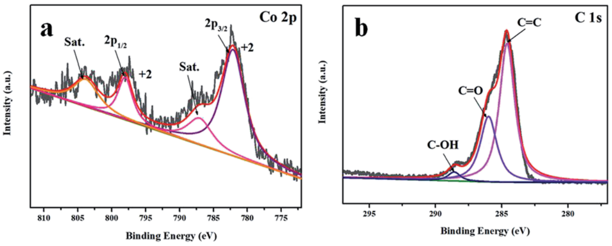

Fig. 4 XPS spectra for Co 2p (a) and C 1s (b) of 0.5-NiS_2/ZIF-67.

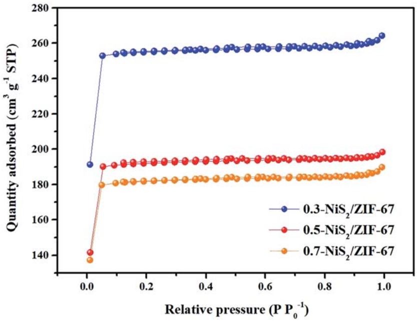

Fig. 5 N_2 adsorption/desorption isotherms of NiS_2/ZIF-67.

Fig. S5† shows the FT-IR spectra results of four different materials. The vibrational bands within the range of 600–1500 cm^{-1} should be assigned to ZIF-67, and the composites possesses the characteristic stretching and bending patterns of the imidazole ring. The stretching vibrational peak at 1629 cm^{-1} corresponds to the stretching mode of C=N in 2-MIM. Meanwhile, the band at 3134 cm^{-1} can be ascribed to the stretching mode of C–H from the aromatic ring and the aliphatic chain of 2-MIM.[52] In addition, the peak intensities of 0.3-NiS_2/ZIF-67, 0.5-NiS_2/ZIF-67 and 0.7-NiS_2/ZIF-67 decreased successively, which also proved that the relative content of ZIF-67 continuously decreased. Because of the ordinary electrochemical performance and stability of ZIF-67 and NiS_2, different amounts of introduction lead to differences in the morphology and performance.

The description of the synthesis process of the NiS_2/ZIF-67 composite is arranged as follows (Scheme 1). Firstly, urea is used to create an alkaline environment, and NiS_2 is synthesized from nickel nitrate and L-cysteine by hydrothermal method. After that, NiS_2 is dispersed in methanol and thoroughly mixed with the added cobalt nitrate. In this process, upon adding 2-methylimidazole solution, the Co^{2+} dispersed on the surface of NiS_2 reacts with 2-methylimidazole to form a ZIF-67 layer. ZIF-67 has a coating effect on NiS_2, and a NiS_2/ZIF-67 composite material is subsequently formed. By controlling the dosage of the nickel source, the ratio of nickel to cobalt can be controlled, which strongly affects the electrochemical performance of the composite material.

3.2 Electrochemical performances

To explore the electrochemical performances of NiS_2, ZIF-67 and NiS_2/ZIF-67 were studied by CV and GCD with a three-electrode system in 2 M KOH electrolyte. As depicted in Fig. 6a, the representative CV curves of 0.5-NiS_2/ZIF-67 were detected in the range from 5 to 50 mV s^{-1} with a potential window of 0–0.5 V. The cyclic voltammograms of the other composites are displayed in Fig. S6.† At different scanning rates, a pair of redox peaks is observed, indicating that a reversible Faraday reaction occurs in the electrochemical charge–discharge process. Although the combined area of the CV curve expands, the peak current increases and its shape does not significantly change. The results show that the electrode material has the advantages of fast ion and electron transfer, high reversibility and large rate capacity.[55]

Fig. 6b shows the CV curves of 0.3-NiS_2/ZIF-67, 0.5-NiS_2/ZIF-67, 0.7-NiS_2/ZIF-67, ZIF-67 and NiS_2 at 10 mV s^{-1}. Importantly, the larger the integral area of the CV curve, the better the capacitance performance of the electrode material.[56] Obviously, 0.5-NiS_2/ZIF-67 has the largest comprehensive area, so it could be preliminarily inferred that the specific capacitance of the NiS_2 material is increased through the composite with ZIF-67. The large CV areas of the 0.5-NiS_2/ZIF-67 composites strongly

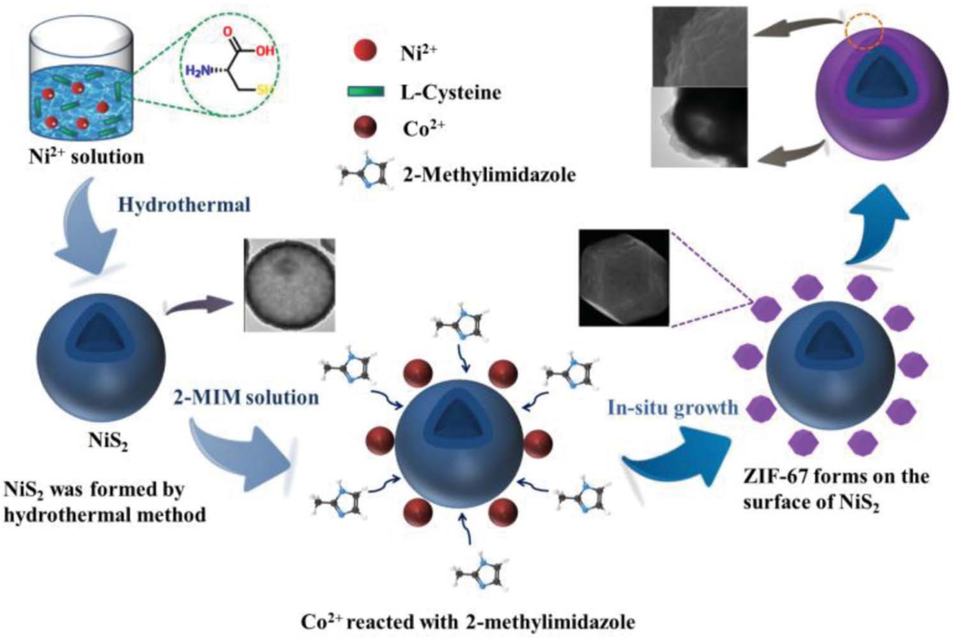

Scheme 1 Schematic illustration of the fabrication process of NiS_2/ZIF-67.

suggest that its specific capacitance is superior to that of other materials.

In order to further appraise the electrochemical performance, GCD detection under different current densities was carried out, as shown in Fig. S7.† Fig. 6c shows the charge–discharge curves of NiS_2/ZIF-67 in contrast with NiS_2 and ZIF-67 at 1 A g^{-1}. The discharge time of 0.5-NIS_2/ZIF-67 composite is obviously longer than that of other materials, and the specific capacitances for 0.3-NiS_2/ZIF-67, 0.5-NiS_2/ZIF-67 and 0.7-NiS_2/ZIF-67 are 672.0, 1297.9 and 593.8 F g^{-1} at 1 A g^{-1}, respectively. Meanwhile, the specific capacitances of ZIF-67 and NiS_2 are 74.7 and 384.0 F g^{-1}, respectively. The specific capacitance of each material displayed by GCD is also in line with the CV measurement results. Through the combination of NiS_2 and the ZIF-67 materials, the specific capacitances of NiS_2 and ZIF-67 have been greatly improved. The addition of ZIF-67 also affects the specific capacitance of the composite. Combined with the previous characterization, it can be found that the excellent morphology of 0.5-NiS_2/ZIF-67 leads to its highest specific capacitance.

Moreover, the specific capacities of the NiS_2, ZIF-67 and NiS_2/ZIF-67 composites were calculated at different current densities,[57] and the results are shown in Fig. 6d. The calculated values are shown in Table S1.† The specific capacitance of 0.5-NiS_2/ZIF-67 is apparently higher than that of 0.3-NiS_2/ZIF-67 and 0.7-NiS_2/ZIF-67. It is worth noting that the specific capacitance retention of NiS_2 is only 7.0% at 10 A g^{-1}. However, the retention rate of the composite with ZIF-67 increased to 27.1% (0.5-NiS_2/ZIF-67).

Fig. 7a shows the Nyquist diagram of the three electrodes to illustrate the impedance characteristics of the samples. The Nyquist diagram of the electrode material for the redox supercapacitors typically consists of a semicircle in the high frequency region that is associated with the Faraday reaction, and a straight line in the low frequency region that is associated with the Warburg impedance.[58,59] According to the equivalent circuit model, the electrode system consists of the electrolyte solution resistance (R_e), Faraday charge transfer resistance (R_{ct}) related to electron transfer, Warburg impedance (Z_w) during ion diffusion and the double-layer capacitance (CPE) at the electrode/electrolyte interface. The parameters were fitted by Zview software. The R_{ct} values of the 0.3-NiS_2/ZIF-67, 0.5-NiS_2/ZIF-67 and 0.7-NiS_2/ZIF-67 composites are 2.40, 1.65 and 2.66 Ω, respectively. EIS experiments show that 0.5-NiS_2/ZIF-67 has lower charge transfer resistance than the other composites.[60]

The cycling performance of the 0.5-NiS_2/ZIF-67 electrode was assessed by GCD detection for 4000 cycles at 5 A g^{-1} (Fig. 7b). Surprisingly, the specific capacitance retention of 0.5-NiS_2/ZIF-67 was 120.0% after 2000 cycles, and it remained at 110.0% even after 4000 cycles. The capacitance of ZIF-67 and NiS_2 remains only 80.0% and 17.9% after 2000 cycles, respectively. Meanwhile, the electrochemical performance of NiS_2 deteriorated rapidly during the cycle. This indicates that the 0.5-NiS_2/ZIF-67 composites have a long cycle life as the electrode material of the supercapacitor. It can be seen that the electrochemical performance of 0.5-NiS_2/ZIF-67 was greatly improved compared with that of the other materials, such as $Ni(OH)_2$,[31] graphene/NiS_2,[64] and Co/Zn–Ni–MOF//CNTs–COOH.[32] As shown in Fig. S8,† electrochemical impedance spectra experiments were performed on NiS_2 before and after the cycle. It was found that the R_{ct} value was reduced from the previous value of 1.65 Ω to 0.85 Ω. The high cycle property is primarily attributed to the unique coating that formed the core–shell structure. The cladding makes the overall structure of the composite more stable and less prone to deformation. The surface of the material has a ZIF-67 coating layer, which not only improves the active site of

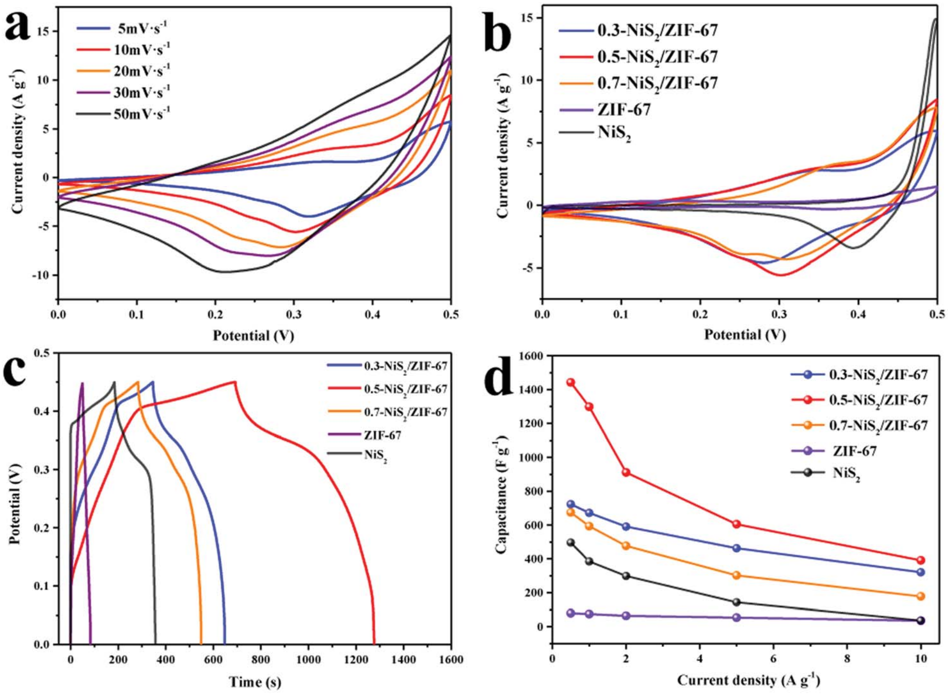

Fig. 6 CV curves of 0.5-NiS_2/ZIF-67 at different scan rates (a) and NiS_2/ZIF-67, ZIF-67 and NiS_2 at a scan rate of 10 mV s^{-1} (b). GCD curves for NiS_2/ZIF-67, ZIF-67 and NiS_2 tested at 1 A g^{-1} (c). Specific capacitance *versus* various current densities for NiS_2/ZIF-67, ZIF-67 and NiS_2 (d).

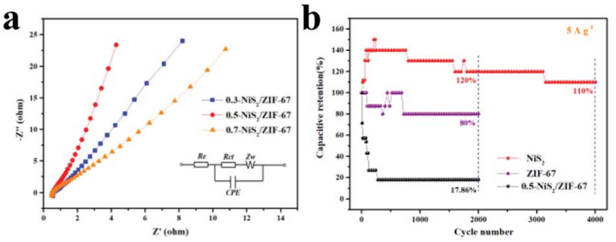

Fig. 7 (a) Nyquist plots of the 0.3-NiS_2/ZIF-67, 0.5-NiS_2/ZIF-67 and 0.7-NiS_2/ZIF-67 composites; the inset shows the equivalent circuit model. (b) Cycling stability performance for NiS_2, ZIF-67 and 0.5-NiS_2/ZIF-67 at 5 A g^{-1}.

the material, but also effectively relieves the large structural contraction and expansion of NiS_2 during the cycle test.

3.3 Electrochemical properties of 0.5-NiS_2/ZIF-67//AC HSC

For further research on the electrochemical property of the 0.5-NiS_2/ZIF-67 composites, a hybrid supercapacitor (HSC) was prepared in 6 M KOH electrolyte with 0.5-NiS_2/ZIF-67 and activated carbon (AC) as the positive and negative electrodes, respectively (Fig. 8a).

Fig. S9a and b† shows the CV and GCD test results of AC. The CV curves at different scanning rates all have the same shape, and the GCD curves at various current densities are smooth straight lines without potential platforms, which is consistent with the behavior of a typical electric double-layer capacitor.[65,66] Moreover, the specific capacitances of AC is 158.4, 137.6, 118.4, 96.0 and 80.0 F g^{-1} at 0.5, 1, 2, 5 and 10 A g^{-1}, respectively.

The mass ratio of the positive and negative electrode is calculated by the following eqn (2):[61,62]

$$\frac{m_+}{m_-} = \frac{C_- \times \Delta V_-}{C_+ \times \Delta V_+} \tag{2}$$

where m, C_s and ΔV are the mass (g), specific capacitance (F g^{-1}) and applied potential window (V). Furthermore, C_+ and C_-, and ΔV_+ and ΔV_- were the specific capacitance and the potential window of the GCD tests of the positive and negative electrodes, respectively. The optimal mass ratio of the electrode materials is $m_{(\mathrm{AC})} : m_{(0.5\text{-}\mathrm{NiS_2/ZIF\text{-}67})} = 4.2 : 1$.

The energy density (E, W h kg^{-1}) and power density (P, W kg^{-1}) of the HSC were determined based on the total mass of the active materials using the following two formulas:[55]

$$E = \frac{1}{2} C \Delta V^2 \tag{3}$$

$$P = \frac{E \times 3600}{\Delta t} \tag{4}$$

where C (F g^{-1}) was the specific capacitance of the HSC calculated from the GCD curves based on the total mass of the active materials on both electrodes, and ΔV (V) and Δt (s) were the potential range and the discharge time of the assembled device obtained from the GCD tests, respectively.

According to the CV curves of the electrodes with two voltage windows of 0 to 0.5 and −1.0 to 0 V obtained in a separate three-electrode configuration (Fig. 8b), it could be expected that the HSC device would provide a stable operating voltage of 1.5 V. Fig. 8c shows the CV curves of the device at different scanning rates in the range of 5–50 mV s^{-1} in a potential window of 0–

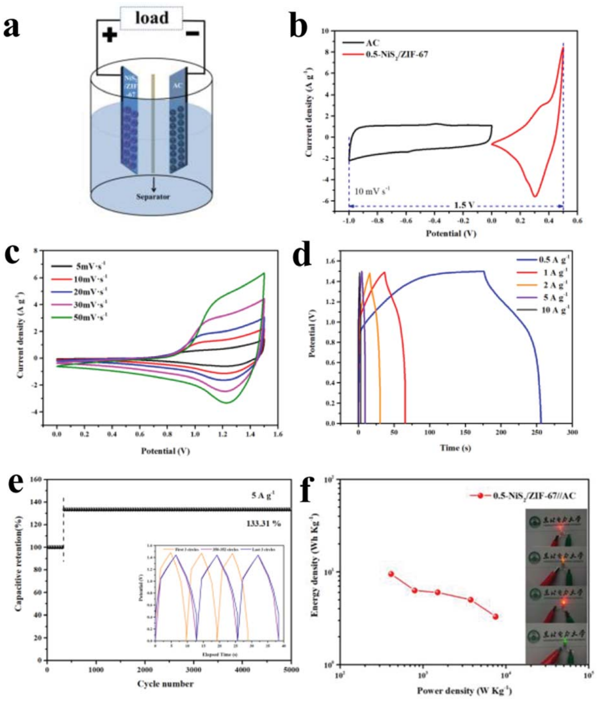

Fig. 8 (a) Schematic illustration of the 0.5-NiS$_2$/ZIF-67//AC HSC. (b) CV curves of the 0.5-NiS$_2$/ZIF-67 and AC electrodes tested at 10 mV s^{-1} in a three-electrode system. Electrochemical performance of the 0.5-NiS$_2$/ZIF-67//AC HSC: (c) CV curves, (d) GCD curves, (e) cycling performance at 5 A g^{-1}, and (f) Ragone plot correlating *E* and *P*; the insets show pictures of the LEDs powered by the 0.5-NiS$_2$/ZIF-67//AC HSC.

1.5 V. The CV curves remain in the same shape even at high scanning rates, which fully demonstrates the advantages of energy storage devices, such as the excellent electrical performance and chemical charge storage performance.[67] In addition, these CV curves show similar twisted rectangular shapes, indicating the mutual influence of the EDLC type and the faradaic pseudocapacitance type electrodes on the total capacity.[63]

Fig. 8d presents the GCD curves of 0.5-NiS$_2$/ZIF-67//AC HSC at different current densities. After that, the cycle stability of 0.5-NiS$_2$/ZIF-67//AC HSC was further tested at 5 A g^{-1} (Fig. 8e). After 300 cycles, the specific capacitance retention was increased to 133.3%, and this characteristic could be maintained for up to 5000 cycles. The GCD curves in the first 3 cycles, 350–352 cycles and the last 3 cycles are presented in the inset of Fig. 8e.

It could be found that the discharge time was significantly improved after 350 cycles. The cycles start after 350 times and the last 3 cycles almost overlap each other, which further demonstrate that the device has excellent cycle stability and application potential. As can be seen from the Ragone plot (Fig. 8f), the energy density of 0.5-NiS$_2$/ZIF-67//AC HSC at 411.1 W kg^{-1} is 9.5 W h kg^{-1}.

In order to reflect the actual working performance of the 0.5-NiS$_2$/ZIF-67//AC HSC device, the two HSCs were connected in series to illuminate commercial yellow light-emitting diodes (LEDs, 2.0–2.2 V) for more than 30 minutes (Fig. 8f illustration). Moreover, the red and green LEDs could be lit.

4. Conclusions

In summary, the NiS$_2$/ZIF-67 composite was prepared by *in situ* growth of ZIF-67 *via* static reaction using NiS$_2$ hollow spheres as the carrier, which was used as electrode materials for supercapacitors. In the process of charging–discharging, the ZIF-67 coating significantly not only improved the conductivity, but also limited the deformation of NiS$_2$. Compared with pure NiS$_2$, the specific capacitance of 0.5-NiS$_2$/ZIF-67 increased from 384.0 to 1297.8 F g^{-1} at 1 A g^{-1}. After 4000 cycles, the capacitance retention rate of 0.5-NiS$_2$/ZIF-67 at 1 A g^{-1} was 110%, which also demonstrated the good cycle stability (the capacitance retention rates of NiS$_2$ and ZIF-67 are only 17.6% and 80.0% after 2000 cycles). Additionally, the corresponding 0.5-NiS$_2$/ZIF-67//AC HSC achieved an energy density of 9.5 W h kg^{-1} at 411.1 W kg^{-1} and possessed excellent electrochemical cycling stability after 5000 cycles. This study demonstrates a mild and easy way to synthesize coating forming core–shell composites with excellent electrochemical properties and application potential in supercapacitors.

Conflicts of interest

There are no conflicts of interest to declare.

Acknowledgements

This work was supported by the National Natural Science Foundation of China (51972049 and 52073010) and the Projects of the Science and Technology Department of Jilin Province (JJKH20220123KJ).

Notes and references

1 A. Kostopoulou, E. Kymakis and E. Stratakis, Perovskite nanostructures for photovoltaic and energy storage devices, *J. Mater. Chem. A*, 2018, **6**, 9765–9798.

2 F. Liu, L. L. Zeng, Y. K. Chen, R. T. Zhang, R. Q. Yang, J. B. Pang, L. H. Ding, H. Liu and W. J. Zhou, Ni–Co–N hybrid porous nanosheets on graphene paper for flexible and editable asymmetric all-solid-state supercapacitors, *Nano Energy*, 2019, **61**, 18–26.

3 S. Choi, H. Lee, R. Ghaffari, T. Hyeon and D. H. Kim, Recent advances in flexible and stretchable bio-electronic devices integrated with nanomaterials, *Adv. Mater.*, 2016, **28**, 4203–4218.

4 C. K. Sun, X. Zhang, C. Li and K. Wang, A safe, low-cost and high-efficiency presodiation strategy for pouch-type sodium-ion capacitors with high energy density, *J. Energy Chem.*, 2021, **64**, 442–450.

5 J. R. Miller and P. Simon, Electrochemical capacitors for energy management, *Science*, 2008, **321**, 651–652.

6 J. M. Wang, Z. Liu, Y. Zheng, L. Cui, W. R. Yang and J. Q. Liu, Recent advances in cobalt phosphide based materials for energy-related applications, *J. Mater. Chem. A*, 2017, **5**, 22913–22932.

7 D. P. Dubal, O. Ayyad, V. Ruiz and P. Gomez-Romero, Hybrid energy storage: the merging of battery and supercapacitor chemistries, *Chem. Soc. Rev.*, 2015, **44**, 1777–1790.

8 Z. Luo, C. Liu and S. Fan, A super compact self-powered device based on paper-like supercapacitors, *J. Mater. Chem. A*, 2019, **7**, 3642–3647.

9 D. H. Kusumawati, N. P. Putri, Asnawi, T. S. Dewi and Munasir, Porosity characteristics and electrochemical performance of rGO coconut shell as supercapacitor electrodes, *J. Phys.: Conf. Ser.*, 2020, **1491**, 012058.

10 K. Mensah-Darkwa, C. Zequine, P. Kahol and R. Gupta, Supercapacitor energy storage device using biowastes: a sustainable approach to green energy, *Sustainability*, 2019, **11**(2), 414.

11 Y. K. Yasun, A. R. Upendra and K. S. Jang, Hybrid supercapacitors based on metal organic frameworks using *p*-phenylenediamine building block, *Chem. Eng. J.*, 2019, **361**, 1235–1244.

12 H. Jia, Q. Li, C. Li, Y. Y. Song, H. R. Zheng, J. G. Zhao, W. Y. Zhang, X. M. Liu, Z. L. Liu and Y. Liu, A novel three-dimensional hierarchical $NiCo_2O_4/Ni_2P$ electrode for high energy asymmetric supercapacitor, *Chem. Eng. J.*, 2018, **354**, 254–260.

13 H. J. Yan, J. W. Bai, M. R. Liao, Y. He, Q. Liu, J. Y. Liu, H. S. Zhang, Z. S. Li and J. Wang, One-step synthesis of Co_3O_4/graphene aerogels and their all-solid-state asymmetric supercapacitor, *Eur. J. Inorg. Chem.*, 2017, **8**, 1143–1152.

14 S. H. Zheng, Z. S. Wu, S. Wang, H. Xiao, F. Zhou, C. L. Sun, X. H. Bao and H. M. Cheng, Graphene-based materials for high-voltage and high-energy asymmetric supercapacitors, *Energy Storage Materials*, 2017, **6**, 70–97.

15 K. Wang, H. Wu and Y. Meng, Conducting polymer nanowire arrays for high performance supercapacitors, *Small*, 2014, **114**(17), 14–31.

16 H. Pang, Q. Lu, Y. Zhang, Y. Li and F. Gao, Selective synthesis of nickel oxide nanowires and length effect on their electrochemical properties, *Nanoscale*, 2010, **2**, 920–922.

17 B. P. Reddy, K. Mallikarjuna, M. Kumar, M. C. Sekhar, Y. Suh and S. H. Park, Highly porous metal organic framework derived NiO hollow spheres and flowers for oxygen evolution reaction and supercapacitors, *Ceram. Int.*, 2020, **47**(3), 3312–3321.

18 Z. Fan, J. Yan, T. Wei, L. Zhi, G. Ning, T. Li and F. Wei, Asymmetric supercapacitors based on graphene/MnO_2 and activated carbon nanofiber electrodes with high power and energy density, *Adv. Funct. Mater.*, 2011, **21**(12), 2366–2375.

19 S. Chen, J. Zhu, X. Wu, Q. Han and X. Wang, Graphene oxide–MnO_2 nanocomposites for supercapacitors, *ACS Nano*, 2010, **4**(5), 2822–2830.

20 U. M. Patil, K. V. Gurav and V. J. Fulari, Characterization of honeycomb-like "β-$Ni(OH)_2$" thin films synthesized by chemical bath deposition method and their supercapacitor application, *J. Power Sources*, 2009, **188**(1), 338–342.

21 Z. Sun and X. Lu, A solid-state reaction route to anchoring $Ni(OH)_2$ nanoparticles on reduced graphene oxide sheets for supercapacitors, *Ind. Eng. Chem. Res.*, 2012, **51**(30), 9973–9979.

22 J. Wang, J. Li, Y. Liu, M. Wang and H. Cui, Branched nanosheets-interlaced structure of Co/Co-doped $Ni(OH)_2$ originating from $Ni_3(NO_3)_2(OH)_4$ template with significantly boosted electrochemical performance, *J. Mater. Sci.*, 2021, **56**(4), 1–13.

23 Q. Cheng, J. Tang, N. Shinya and L. C. Qin, $Co(OH)_2$ nanosheet-decorated graphene–CNT composite for supercapacitors of high energy density, *Sci. Technol. Adv. Mater.*, 2014, **15**, 14206–14211.

24 X. Yue, R. Hu, D. Zhu, J. Qi and Y. Sui, Controlled synthesis and formation mechanism of flower-like CuS/NiS microspheres for supercapacitors, *Surf. Interfaces*, 2021, **22**, 100871.

25 Y. Lu, X. Liu, W. Wang, J. Cheng, H. Yan and C. Tang, Hierarchical, porous CuS microspheres integrated with carbon nanotubes for high-performance supercapacitors, *Sci. Rep.*, 2015, **5**, 16584.

26 J. Yang, X. Duan, Q. Qin and W. Zheng, Solvothermal synthesis of hierarchical flower-like β-NiS with excellent electrochemical performance for supercapacitors, *J. Mater. Chem. A*, 2013, **1**(27), 7880–7884.

27 J. Yang, X. Duan, W. Guo, D. Li, H. Zhang and W. Zheng, Electrochemical performances investigation of NiS/rGO composite as electrode material for supercapacitors, *Nano Energy*, 2014, **5**, 74–81.

28 H. Pang, C. Wei, X. Li, G. Li, Y. Ma and S. Li, Microwave-assisted synthesis of NiS_2 nanostructures for supercapacitors and cocatalytic enhancing photocatalytic H_2 production, *Sci. Rep.*, 2014, **4**, 3577.

29 Y. G. Xu, J. Liu and L. B. Kong, Reduced graphene oxide decorated amorphous NiS_2 nanosheets as high-performance anode materials for enhanced sodium-ion hybrid capacitors, *Ionics*, 2021, **27**(8), 1–11.

30 A. K. Mishra and S. Ramaprabhu, Functionalized graphene-based nanocomposites for supercapacitor application, *J. Phys. Chem. C*, 2011, **115**(29), 14006–14013.

31 B. R. Wiston and M. Ashok, Electrochemical performance of hydrothermally synthesized flower-like α-nickel hydroxide, *Vacuum*, 2019, **160**, 12–17.

32 J. Yang, P. Jian, D. Chen, C. Yan and C. Gang, Mixed-metallic MOF based electrode materials for high performance hybrid supercapacitors, *J. Mater. Chem. A*, 2017, **5**, 1094–1102.

33 G. Zhang, B. W. Hao, T. Song, U. Paik and W. L. Xiong, TiO_2 hollow spheres composed of highly crystalline nanocrystals exhibit superior lithium storage properties, *Angew. Chem., Int. Ed.*, 2015, **126**(46), 12798–12801.

34 S. B. Khan, M. Faisal, M. M. Rahman, I. A. Abdel-Latif, A. A. Ismail, K. Akhtar, A. Al-Hajry, A. M. Asiri and K. A. Alamry, Highly sensitive and stable phenyl hydrazine chemical sensors based on CuO flower shapes and hollow spheres, *New J. Chem.*, 2013, **37**, 1098–1104.

35 Y. Wu, Y. Ming, S. Lin and W. Shi, Flexible yolk-shelled $NiCo_2S_4$ hollow spheres/RGO film electrodes for efficient supercapacitive energy storage, *New J. Chem.*, 2018, **42**, 16174–16182.

36 M. Hua, S. Zhang, B. Pan, W. Zhang, L. Lv and Q. Zhang, Heavy metal removal from water/wastewater by nanosized metal oxides: a review, *J. Hazard. Mater.*, 2012, **211**, 317–331.

37 C. Wei, C. Cheng, J. Zhao, Y. Wang, Y. Cheng and Y. Xu, NiS hollow spheres for high-performance supercapacitors and non-enzymatic glucose sensors, *Chem.–Asian J.*, 2015, **10**(3), 679–686.

38 F. Saleki, A. Mohammadi, S. E. Moosavifard, A. Hafizi and M. R. Rahimpour, MOF assistance synthesis of nanoporous double-shelled $CuCo_2O_4$ hollow spheres for hybrid supercapacitors, *J. Colloid Interface Sci.*, 2019, **556**, 83–91.

39 C. Wei, C. Cheng, Y. Cheng, Y. Wang, Y. Xu, W. Du and H. Pang, Comparison of NiS_2 and α-NiS hollow spheres for supercapacitors, non-enzymatic glucose sensors and water treatment, *Dalton Trans.*, 2015, **44**, 17278–17285.

40 B. T. Zhu, Z. Wang, S. Ding, J. S. Chen and X. W. Lou, Hierarchical nickel sulfide hollow spheres for high performance supercapacitors, *RSC Adv.*, 2011, **1**(3), 397–400.

41 W. Yu, X. B. Jiang, S. J. Ding and B. Q. Li, Preparation and electrochemical characteristics of porous hollow spheres of NiO nanosheets as electrodes of supercapacitors, *J. Power Sources*, 2014, **256**, 440–448.

42 Y. Zhao, Y. Li, D. Zhang, S. Song, J. Wang, Y. J. Ke, R. Guo, Y. B. Ding and X. D. Zhu, Effect of reaction time on the performance of Co_3O_4 electrode materials for high performance supercapacitors, *J. Nanoelectron. Optoelectron.*, 2020, **15**(12), 1429–1435.

43 W. Ma, Y. Guo, X. Liu, D. Zhang, T. Liu, R. Ma, K. Zhou and G. Qiu, Nickel dichalcogenide hollow spheres: Controllable fabrication, structural modification, and magnetic properties, *Chem.–Eur. J.*, 2013, **19**, 15467–15471.

44 J. Zhang, H. Hu, Z. Li and X. Lou, Double-shelled nanocages with cobalt hydroxide inner shell and layered double hydroxides outer shell as high-efficiency polysulfide mediator for lithium–sulfur batteries, *Angew. Chem.*, 2016, **128**(12), 4050–4054.

45 P. X. Sun, W. D. He, H. C. Yang, R. Y. Cao, J. M. Yin, C. G. Wang and X. J. Xu, Hedgehog-inspired nanostructures for hydrogel-based all-solid-state hybrid supercapacitors with excellent flexibility and electrochemical performances, *Nanoscale*, 2018, **10**, 19004–19013.

46 F. Zheng, M. Guo and M. Zhang, Hydrothermal preparation and optical properties of orientation-controlled WO_3 nanorod arrays on ITO substrates, *CrystEngComm*, 2013, **15**, 277–284.

47 M. Lu, X. P. Yuan, X. H. Guan and G. S. Wang, Synthesis of nickel chalcogenide hollow spheres using an L-cysteine-assisted hydrothermal process for efficient supercapacitor electrodes, *J. Mater. Chem. A*, 2017, **5**, 3621–3627.

48 J. F. Qian, F. Sun and L. Z. Qin, Hydrothermal synthesis of zeolitic imidazolate framework-67 (ZIF-67) nanocrystals, *Mater. Lett.*, 2012, **82**(1), 220–223.

49 T. Q. Peng, H. Yi, P. Sun, Y. T. Jing, R. J. Wang, H. W. Wang and X. F. Wang, In situ growth of binder-free CNTs@Ni–Co–S nanosheets core/shell hybrids on Ni mesh for high energy density asymmetric supercapacitors, *J. Mater. Chem. A*, 2016, **4**, 8888–8897.

50 J. Qin, S. Wang and X. Wang, Visible-light reduction CO_2 with dodecahedral zeolitic imidazolate framework ZIF-67 as an efficient co-catalyst, *Appl. Catal., B*, 2017, **209**, 476–482.

51 M. Mansuer, L. Miao, Y. Qin, Z. Song, D. Zhu, H. Duan and L. Gan, Trapping precursor-level functionalities in hierarchically porous carbons prepared by a pre-stabilization route for superior supercapacitors, *Chin. Chem. Lett.*, 2022, DOI: 10.1016/j.cclet.2022.03.027.

52 S. Sundriyal, V. Shrivastav, H. Kaur, S. Mishra and A. Deep, High-performance symmetrical supercapacitor with a combination of a ZIF-67/rGO composite electrode and a redox additive electrolyte, *ACS Omega*, 2018, **3**(12), 17348–17358.

53 Z. Song, L. Miao, L. Ruhlmann, Y. Lv, D. Zhu, L. Li and M. Liu, Self-assembled carbon superstructures achieving ultra-stable and fast proton-coupled charge storage kinetics, *Adv. Mater.*, 2021, **33**(49), 2104148.

54 H. Duan, Z. Song, L. Miao, L. Li, D. Zhu, L. Gan and M. Liu, Unraveling the role of solvent–precursor interaction in fabricating heteroatomic carbon cathode for high-energy-density Zn-ion storage, *J. Mater. Chem. A*, 2022, **10**(18), 9837–9847.

55 L. Yang, M. Huang, M. Lu, X. H. Guan, X. Guan, G. S. Wang and B. Jia, Facile design and synthesis of nickle-molybdenum oxide/sulfide composites with robust microsphere structure for high-performance supercapacitors, *Chem. Eng. J.*, 2019, **364**, 462–474.

56 Z. Ma, H. Zhang, Y. Zhang, J. Zhang and Z. Li, Electrochemical characteristics of nanostructured NiO plates hydrothermally treated on nickel foam for Li-ion storage, *Electrochim. Acta*, 2015, **176**, 1427–1433.

57 R. A. Patil, C. P. Chang, R. S. Devan, Y. Liou and Y. R. Ma, Impact of nanosize on supercapacitance: study of 1D nanorods and 2D thin-films of nickel oxide, *ACS Appl. Mater. Interfaces*, 2016, **8**, 9872–9880.

58 Y. Li, J. Xu, H. Liu, Y. Liu, M. Wang, J. Li and H. Cui, Surface topography control of NiS/Ni_3S_4 nanosheets for the promotion of electrochemical performance, *J. Sol-Gel Sci. Technol.*, 2018, **87**, 546–553.

59 H. Tang, J. Wang, H. Yin, H. Zhao, D. Wang and Z. Tang, Growth of polypyrrole ultrathin films on MoS_2 monolayers as high-performance supercapacitor electrodes, *Adv. Mater.*, 2014, **27**, 1117–1123.

60 L. Zhu, C. K. N. Peh, T. Zhu, Y. F. Lim and G. W. Ho, Bifunctional 2D-on-2D MoO_3 nanobelt/$Ni(OH)_2$ nanosheets for supercapacitor-driven electrochromic energy storage, *J. Mater. Chem. A*, 2017, **5**, 8343–8351.

61 C. G. Wang, X. Xu and T. Zhai, Hierarchical $CuCo_2O_4$@nickel-cobalt hydroxides core/shell nanoarchitectures for high-performance hybrid supercapacitors, *Sci. Bull.*, 2017, **62**, 1122–1131.

62 X. Xu, P. Sun, W. He, H. Yang, R. Cao, J. Yin, C. Wang and X. Xu, Hedgehog-inspired nanostructures for hydrogel-based all-solid-state hybrid supercapacitors with excellent

flexibility and electrochemical performance, *Nanoscale*, 2018, **10**, 19004–19013.

63 G. Li, H. Cai, X. Li, J. Zhang, D. Zhang, Y. Yang and J. Xiong, Construction of hierarchical $NiCo_2O_4$@Ni-MOF hybrid arrays on carbon cloth as superior battery-type electrodes for flexible solid-state hybrid supercapacitors, *ACS Appl. Mater. Interfaces*, 2019, **11**(41), 37675–37684.

64 X. Li, J. Shen, N. Li and M. Ye, Template-free solvothermal synthesis of NiS_2 microspheres on graphene sheets for high-performance supercapacitors, *Mater. Lett.*, 2015, **139**, 81–85.

65 Z. Song, L. Miao, H. Duan, L. Ruhlmann, Y. Lv, D. Zhu and M. Liu, Anionic co-insertion charge storage in dinitrobenzene cathodes for high-performance aqueous zinc–organic batteries, *Angew. Chem.*, 2022, **61**, e202208821.

66 Y. Qin, L. Miao, M. Mansuer, C. Hu, Y. Lv, L. Gan and M. Liu, Spatial confinement strategy for micelle-size-mediated modulation of mesopores in hierarchical porous carbon nanosheets with an efficient capacitive response, *ACS Appl. Mater. Interfaces*, 2022, **14**, 33328–33339.

67 W. Du, L. Miao, Z. Song, X. Zheng, Y. Lv, D. Zhu and M. Liu, Kinetics-driven design of 3D VN/MXene composite structure for superior zinc storage and charge transfer, *J. Power Sources*, 2022, **536**, 231512.